Numerical Simulation of contrail formation on the Common Research Model wing/body/engine configuration

Emmanuel Montreuil, Weeded Ghedhaifi, Vivien Chmielaski, Francois Vuillot, Fabien Gand, Adrien Loseille

Numerical Simulation of contrail formation on the Common Research Model wing/body/engine configuration

E. Montreuil[1], W. Ghedhaïfi[2], Vivien Chmielarski[3], François Vuillot[4] and Fabien Gand[5]
ONERA, Palaiseau (91), France

and

A. Loseille[6]
INRIA, Saclay (91), France

Aircraft contrails may contribute to the global radiative forcing. In this context, the investigation of contrail formation in the near field of an aircraft may be helpful in developing strategies to reduce undesirable impacts. Contrail formation is also a complex topic, since several physical processes are involved, covering a large range of space and time scales, from the engine exit to the atmospheric global scale. In the near field of the aircraft, contrail formation is mainly dominated by microphysics and mixing processes between the propelling jets and the external flow (the so called jet-vortex interaction). In this study, three-dimensional Reynolds-Averaged Navier–Stokes (RANS) simulations of contrails produced by the Common Research Model wing/body/engine configuration during cruise flights is performed. In the present work, a dedicated internal nozzle geometry has been designed to replace the through flow nacelle of the original CRM configuration. Thus, the engine core and bypass flows are actually computed in the simulations, which allows several parametrical studies and avoids using parameterizations to describe the plume's dilution. The objective is to simulate the early development of contrails in a fresh plume whose dilution is obtained with a spatial simulation of jet/vortex interaction. A coupling is carried out with a chemical and a microphysical model implemented in the unstructured Navier-Stokes CFD code CEDRE to simulate particle growth using an Eulerian approach. The implemented microphysics model can simulate water condensation onto soot particles, taking into account their activation by adsorption of sulfur species. In this context, an adaptation grid mesh procedure has been used in order to generate an optimized unstructured mesh in the fluid zone of interest (i.e. vortex wake and jet exhaust).

I. Introduction

The continuous growth in air traffic over the past decades has raised environmental concerns regarding the impact of aircraft-engine emissions. The consequences of such emissions have been largely studied in recent years, but the level of scientific understanding of the role played by contrails and the induced cirrus clouds remains poor [1][2]. Contrail-formation conditions can be fairly well determined from a thermodynamic point of view using the revised Schmidt–Appleman criterion [3]. Based on the physical laws of conservation, the criterion provides the atmospheric threshold temperature so that water saturation is reached in the expanding plume at a given ambient relative humidity.

The environmental impact is also related to the contrail optical thickness, which depends on the actual microphysical properties of the plume and the atmospheric environment, along with other parameters. The

[1] Research engineer, Department Multi-Physic for Energetics, Emmanuel.montreuil@onera.fr.
[2] Research engineer, Department Multi-Physic for Energetics, Weeded.ghedhaifi@onera.fr.
[3] PhD student, Department Multi-Physic for Energetics, vivien.chmielarski@onera.fr.
[4] Research engineer, Department Multi-Physic for Energetics, francois.vuillot@onera.fr.
[5] Research engineer, Department Aerodynamics Aeroelasticity Acoustics, fabien.gand@onera.fr.
[6] Scientist researcher, GAMMA3 project, Adrien.loseille@inria.fr.

knowledge of ice-crystal number density as well as their size distribution in water-supersaturated aircraft plumes is therefore highly desirable in order to refine contrail and contrail–cirrus atmospheric impact assessments. Direct in-flight measurements can provide relevant information on plume microphysical properties [4][5] but are difficult to achieve from a technical point of view. Besides, field campaigns require a large set of instruments and partners ranging from scientists to air traffic controllers.

Contrail formation and its evolution to a contrail cirrus, on length scales up to kilometers from the engine and up to hours from the emission times, are complex processes, leading to a spatially inhomogeneous distribution of gaseous constituents and primary particles, whose evolution is controlled by thermodynamic conditions and aircraft parameters.

The detailed features of contrail microphysics was recently investigated with a high-fidelity unsteady numerical approach: the large eddy simulation (LES). This method is now recognized as a powerful tool for interpreting turbulent mixing associated with microphysics during the jet/vortex phase [6][7], the vortex phase and dissipation regimes [8][9][10][11], up to the aging contrail-induced cirrus phase [9]. However, a detailed chemistry is not taking into account.

In Ref. [12], an extensive study of the effect of aircraft type on contrail evolution was carried out but generally used parameterized initialization of the wing-tip vortices and its interaction with the engine jets. However, this does not provide for accurately taking into consideration the actual aircraft and engine geometries, including the interaction with detailed chemistry and gas/particle physics.

We recently reported the results of three-dimensional Reynolds-averaged Navier-Stokes (RANS) numerical simulations of contrails generated by a commercial aircraft in cruise conditions [13][14]. This work was based on an original coupled aerodynamics/microphysics approach on an aircraft of realistic geometry, and pointed to the role of ambient relative humidity on ice crystal growth in the plume. This first achievement did not, however, account for plume gas phase chemistry and hence, considered only limited gas-particle interactions through water vapor deposition/evaporation processes, similarly to most CFD plume microphysical models.

The following sections introduce the different parts of the model, fluid flow, chemistry and microphysics models. The mesh adaptation procedure is detailed. The numerical setup is then described and results are finally presented.

II. Model overview

A. Fluid-Flow Solver

The CEDRE numerical code used for this study is a parallel, three-dimensional, multi-species, compressible Navier–Stokes solver [17]. The numerical method is based on a cell-centered finite-volume approach for general unstructured grids, especially appropriate when complex geometries are used. The mass-conservation equations related to the 3-D compressible Navier–Stokes equations in CEDRE are:

$$\frac{\partial}{\partial t}\left(\rho y_k\right)+\frac{\partial}{\partial x_j}\left(\rho u_j y_k\right)=\frac{\partial}{\partial x_j}\left(\rho D_k\frac{\partial y_k}{\partial x_j}\right)+\dot{w}_k \qquad (1)$$

$$\frac{\partial}{\partial t}\left(\rho u_i\right)+\frac{\partial}{\partial x_j}\left(\rho u_i u_j\right)=-\frac{\partial p}{\partial x_i}-\rho g\delta_{i3}+\frac{\partial}{\partial x_j}\left(\mu S_{ij}^d\right) \qquad (2)$$

$$\frac{\partial}{\partial t}\left(\rho e_t\right)+\frac{\partial}{\partial x_j}\left(\rho u_j h_t\right)=\frac{\partial}{\partial x_j}\left(\rho c_p\kappa\frac{\partial T}{\partial x_j}+\sum_k h_k D_k\frac{\partial y_k}{\partial x_j}+\mu S_{ij}^d u_i\right) \qquad (3)$$

where the variables are velocity vector $\left(u_1,u_2,u_3\right)^T$; pressure p; total energy $e_t=e+u_i u_i/2$, where e is the internal energy; total enthalpy $h_t=e_t+p/\rho$; temperature T; the deviator strain-rate tensor $S_{ij}^d=\left(\frac{\partial u_i}{\partial x_j}+\frac{\partial u_j}{\partial x_i}\right)-\frac{2}{3}\frac{\partial u_l}{\partial x_l}\delta_{ij}$; and dynamical viscosity μ. The species are governed by their mass fraction y_k, their diffusion coefficient in the mixture D_k, and their mass transfer rate $\dot{w}_k$. The thermal diffusivity is represented by κ.

A high-resolution spatial RANS method was used, where the equations are averaged so that any variable Φ may be decomposed into a mean part $\overline{\Phi}$ and a fluctuation part Φ', with $\Phi=\overline{\Phi}+\Phi'$. For compressible flows, a density-

weighted, time-average decomposition (also called Favre average) is used: variables are then defined as $\tilde{\Phi} = \overline{\rho\Phi}\big/\overline{\rho}$ and $\Phi = \tilde{\Phi} + \Phi''$. The new system of equations is then:

$$\frac{\partial}{\partial t}\left(\overline{\rho}\tilde{y}_k\right) + \frac{\partial}{\partial x_j}\left(\overline{\rho}\tilde{u}_j\tilde{y}_k\right) = \frac{\partial}{\partial x_j}\left(\overline{\rho}D_k\frac{\partial\tilde{y}_k}{\partial x_j} - \overline{\rho}\widetilde{u_j''y_k''}\right) + \overline{\dot{w}}_k \qquad (4)$$

$$\frac{\partial}{\partial t}\left(\overline{\rho}\tilde{u}_i\right) + \frac{\partial}{\partial x_j}\left(\overline{\rho}\tilde{u}_i\tilde{u}_j\right) = -\frac{\partial\overline{p}}{\partial x_i} - \overline{\rho}g\delta_{i3} + \frac{\partial}{\partial x_j}\left(\mu\tilde{S}_{ij}^d - \overline{\rho}\widetilde{u_i''u_j''}\right) \quad (5)$$

$$\begin{aligned}\frac{\partial}{\partial t}\left(\overline{\rho}\tilde{e}_t\right) + \frac{\partial}{\partial x_j}\left(\overline{\rho}\tilde{u}_j\tilde{h}_t\right) = \\ \frac{\partial}{\partial x_j}\left(\overline{\rho}c_p\kappa\frac{\partial\overline{T}}{\partial x_j} - \overline{\rho}\widetilde{u_j"T"} + \sum_k\tilde{h}_k\overline{\rho}D_k\frac{\partial\tilde{y}_k}{\partial x_j} - \sum_k\tilde{h}_k\overline{\rho}\widetilde{u_j"y_k"} + 2\mu\tilde{S}_{ij}^d\tilde{u}_i - \overline{\rho}\widetilde{u_i"u_j"}\tilde{u}_i\right)\end{aligned} \qquad (6)$$

The Reynolds tensor (i.e. $\widetilde{u_i''u_j''}$) is given by a Boussinesq hypothesis and the two-equation k-w model of Menter with SST correction [18]. The turbulent diffusion fluxes of species and heat (respectively, $\widetilde{u_j''y_k''}$ and $\widetilde{u_j''T''}$) were assessed in analogy with molecular diffusion flux:

$$\widetilde{u_i''u_j''} = -\nu^t\tilde{S}_{ij}^d + \frac{2}{3}k\delta_{ij} \qquad (7)$$

$$\widetilde{u_j''T''} = -\kappa^t\frac{\partial\overline{T}}{\partial x_j} = -\frac{\nu^t}{\mathrm{Pr}^t}\frac{\partial\overline{T}}{\partial x_j} \quad (8)$$

$$\widetilde{u_j''y_k''} = -D_k^t\frac{\partial\tilde{y}_k}{\partial x_j} = -\frac{\nu^t}{\mathrm{Sc}_k^t}\frac{\partial\tilde{y}_k}{\partial x_j} \qquad (9)$$

where the terms ν^t, Pr^t and Sc_k^t correspond to the turbulent eddy viscosity, the turbulent Prandtl number, and the turbulent Schmidt numbers, respectively.

B. Gas-Phase Chemistry

The mass of nonideal combustion products is very low, but the consequences for atmospheric chemistry are significant. When interacting together and with ambient species during the aforementioned mixing process, emitted materials undergo chemical transformations that determine their atmospheric impact by direct or indirect effects involving secondary products. Their concentration depends on various parameters such as the engine type, the fuel composition, the plume dilution and the ambient conditions.

The main gaseous emissions from aircraft engines are carbon dioxide (CO_2) and water vapor ($H_2O^{(g)}$). Minor species are nitrogen oxides (NO_x), carbon oxide (CO) and hydrocarbons, which are regulated. Furthermore, sulfur is found in aircraft fuel at different concentrations. Sulfur products are quite important because they act as aerosol precursors, which can promote homogenous nucleation and form volatile sulfate aerosols. As sulfur products are also expected to activate soot-particle surfaces and enhance contrail formation, it is highly desirable to know the amount of sulfur species in the plume.

A kinetic reaction scheme has been implemented in CEDRE based on the work of Ref. [20][21]. The scheme consists of 23 species and 60 reactions, including SO_x, NO_x and HO_x chemistry. Indeed, the knowledge of the behavior of other species, such as NO_x and HO_x, is also needed, since they play a major role in air quality and climate-change issues, especially through ozone formation. Furthermore, they are also necessary to predict SO_x concentration, since there are many interactions between NO_x, HO_x, and SO_x in the plume.

The equation of evolution of the mass fraction y_k of each species k is given by Eq. (4) in which the source term $\overline{\dot{w}}_k$, corresponding to the mass reaction rate, is assessed with Arrhenius laws. A reversible chemical reaction can then be written as:

$$\sum_{j=1}^{N^r} \upsilon_j^r E_j \xrightleftharpoons{M} \sum_{j=1}^{N'^r} \upsilon_j'^r E_j' \quad (10)$$

where N^r and N'^r are, respectively, the number of reactant and product species in the reaction r; E_j^r and $E_j'^r$ are, respectively, the reactant and product species; and υ_j^r and $\upsilon_j'^r$ are the stoichiometric coefficients of the reactant and product species. Given the pre-exponential factors A_r, the temperature exponents α_r, and the activation temperatures T_{A_r}, the reaction rate is then:

$$\dot{\boldsymbol{\Omega}}_r = A_r^1 T^{\alpha_r^1} \exp\left(-\frac{T_{A_r}^{\alpha_r^1}}{T}\right) \prod_{j=1}^{N} \left[E_j^r\right]^{\upsilon_j^r} - A_r^2 T^{\alpha_r^2} \exp\left(-\frac{T_{A_r}^{\alpha_r^2}}{T}\right) \prod_{j=1}^{N'} \left[E_j'^r\right]^{\upsilon_j'^r} \quad (11)$$

where the subscript *r* refers to the reaction, the superscripts 1 and 2 refer to direct and reverse direction of the reaction, respectively, and the symbol [ ] refers to the concentration in mol/L.

Finally, the mass production rate for the species *k* (i.e. $\dot{\bar{w}}_k$) is obtained from:

$$\dot{\bar{w}}_k = M_k \sum_{r=1}^{n} \upsilon_k^r \dot{\Omega}_r \quad (12)$$

where M_k refers to the species molar mass and *n* refers to the number of considered reactions.

C. Microphysical Model

The plume mixture is assumed to be initially made of exhaust gases and soot particles, while species are considered as ideal gases. Soot particles are assumed to be spherical for the sake of simplicity, as their fractal-like structure is too complex to account for, especially in a CFD code, and the impact of such a property remains difficult to assess.

The freezing process is supposed to be immersion freezing from a thin liquid layer, and we assume that turbulence does not promote ice growth in any particular direction. Therefore, the assumption that soot particles are initially spherical, is a reasonable simplification, although collision processes on aggregates may be enhanced in comparison with spherical particles. Gas and particles (soot and induced ice crystals) are assumed to be in dynamic and thermal equilibrium [14].

Therefore, particles are transported like a passive scalar using an Eulerian approach, the number density per cell calculated with the following transport equation:

$$\frac{\partial}{\partial t}\left(\bar{\rho}\tilde{N}_p\right) + \frac{\partial}{\partial x_j}\left(\bar{\rho}\tilde{u}_j\tilde{N}_p\right) = \frac{\partial}{\partial x_j}\left(D_{diff}\frac{\partial \tilde{N}_p}{\partial x_j} - \widetilde{\bar{\rho}u_j''N_p''}\right) \quad (13)$$

where $\tilde{N}_p$ represents the particle-number density (number of particles per unit volume).

Soot coating with sulfuric acid and sulfur trioxide formed in the plume was enabled by adsorption. We used the chemical kinetics scheme previously described to determine the concentration of the sulfur compounds formed from the sulfur initially in the fuel. The chemical activation process was considered based on the work reported, for instance, in Ref. [15]. The surface covered in sulfur species (referred to as the activated surface) was given by:

$$\theta_a = \frac{\mathscr{N}_A}{4\pi r_s^2 \tilde{N}_p \sigma_0}\left(\left[SO_3^a\right] + \left[H_2SO_4^a\right]\right) \quad (14)$$

where $\mathscr{N}_A$ is Avogadro's number; σ_0 is the number of available sites per unit area of soot particle, taken from Ref. [19]; r_s is the radius of the dry soot; $\left[SO_3^a\right]$ and $\left[H_2SO_4^a\right]$ are the concentration of gaseous sulfur species adsorbed at the soot surface, calculated with Equations (4) and (12) using the specific source terms defined as follows:

$$\begin{cases} \dot{\overline{w}}_X = \alpha_a\left(\overline{T}\right)\pi r_s^2 v_X^{th}\left(\overline{T}\right)\left[X\right]\tilde{N}_p\left(1-\theta_a\right) \\ v_X^{th} = \sqrt{\dfrac{8R\overline{T}}{\pi M_X}} \\ \alpha_a\left(\overline{T}\right) = \begin{cases} 0 \text{ when } \overline{T} \le 420K \\ 1 \text{ when } \overline{T} > 420K \end{cases} \end{cases} \quad (15)$$

where $\alpha_a(\overline{T})$ is sulfur species accommodation coefficient, $v_X^{th}\left(\overline{T}\right)$ is the molecule average thermal speed for species X (X for SO_3 and H_2SO_4), and $\left[X\right]$ is the concentration of gaseous species X in the plume.

The main assumption used in this work is that contrail formation is driven by ice heterogeneous nucleation on chemically activated soot particles. Water-vapor deposition was scaled by the coated fraction θ_{ads}. Growth was assessed with a modified Fick's law dedicated to mass transfer on particles whose radii r_p is of the order of the mean free path λ. The mass transfer rate $\dot{\overline{w}}_{ice}$ $[\mathrm{kg.m^{-3}.s^{-1}}]$ is given by:

$$\dot{\overline{w}}_{ice} = \frac{4\pi\tilde{N}_p\, r_p\, \theta_a D_{vap}\, M_{H_2O}}{R\overline{T}}\left(\overline{p}_{vap} - \overline{p}_{vap}^{sat/ice}\left(r_p\right)\right)G\left(r_p\right)\boldsymbol{\Pi}\left(\overline{p}_{vap}^{sat/liq}, r_p\right) \quad (16)$$

where M_{H_2O} is the water molar mass, R the ideal-gas constant, and D_{vap} the diffusion coefficient of water vapor in air. Furthermore, the mass transfer depends on saturation conditions and, more precisely, on the difference between the water-vapor partial pressure in the plume $\overline{p}_{vap}$ and the saturation vapor pressure above an ice particle of radius r_p $\overline{p}_{vap}^{sat/ice}\left(r_p\right)$. Note that the curvature effect (the so-called Kelvin effect) is accounted for in the definition of $\overline{p}_{vap}^{sat/ice}\left(r_p\right)$. $\tilde{N}_p$ is the particle-number density and r_p is the particle radius. It should be noted that since soot particles are considered monodispersed in size, the induced ice crystal population is also monodisperse within a cell.

The function Π is given by:

$$\boldsymbol{\Pi}\left(\overline{p}_{vap}^{sat/liq}, r_p\right) = \begin{cases} 0 \text{ when } \overline{p}_{vap} \le \overline{p}_{vap}^{sat/liq} \text{ and } r_p = r_s \\ 1 \text{ when } \overline{p}_{vap} \ge \overline{p}_{vap}^{sat/liq} \text{ or } r_p > r_s \end{cases} \quad (17)$$

where $\overline{p}_{vap}^{sat/liq}$ is the saturation vapour pressure above liquid water. The function Π first starts mass transfer onto the dry particles when water liquid saturation is reached in the plume, since this is necessary for contrail formation [16].

III. Mesh adaptation procedure: feflo.a software

The mesh adaptation technique performs surface and volume anisotropic remeshing based on a prescribed Riemannian metric field. The global process sequence is schemed Fig. 1. Such approaches are particularly well suited to shock waves and wakes propagation far from the source as the strong gradients can be captured with a contained mesh density, thus inducing limited numerical additional cost. The complete adaptive algorithm for steady simulations is composed of the following steps as depicted:

1. Compute the fow field (i.e. converge the fow solution on the current mesh);
2. Compute the metric-based error estimate;
3. Generate a unit mesh with respect to these metric fields;
4. Re-project the surface mesh onto the true geometry using the CAD data;
5. Interpolate the flow solution on the new adapted mesh;
6. Goto 1.

Metric-based mesh adaptation is an elegant concept introduced in the pioneering works [22][23]. It (theoretically) allows transforming any unstructured uniform mesh generator into an anisotropic one. This is done by computing the distance in a Riemannian space instead of the classical Euclidean metric space. The adaptive mesh generator aims at creating a unit-mesh (uniform mesh) in this space.

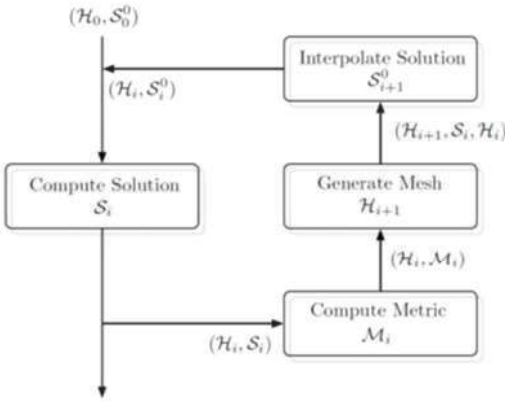

Fig. 1 INRIA mesh adaptation process workflow management scheme

For Step 2, we control the linear interpolation error of the Mach number. This allows deriving a simple anisotropic metric-based estimate [22] by considering an error bound involving a recovered Hessian [24] of the numerical solution. Note that this approach has already demonstrated its efficiency on numerous 3D real-life problems [25][26]. In this paper, instead of classical error equi-distribution issued from an L^{∞} norm, we prefer to control the L^p norm of the interpolation error. Such control allows to recover the order of convergence of the scheme on flows with shocks and to capture of the scales of the numerical solution [24]. Given a numerical solution u_h (density, pressure, mass fraction, …), the point-wise metric tensor is given by:

$$M_{L^p}(u_h) = \det(|H_R(u_h)|)^{\frac{-1}{2p+3}} |H_R(u_h)| \quad (18)$$

where $H_R(.)$ stands for an operator that from u_h recovers some approximated second derivatives of u_h. Then $|H_R(u_h)|$ is deduced from $H_R(u_h)$ by taking the absolute value of the eigen-values of $H_R(u_h)$. Most common operators are deduced from a double L^2 projection or by the use of the Green formula. A numerical review of H_R operators is given in Ref. [27][28]. When applied to a given smooth continuous function u, it has been proven [29] that for any unit-mesh H of Ω_h with respect to M_{L^p} will verify the following bound:

$$\|u - \Pi_h u\|_{L^p(\Omega_h)} \leq C\, N^{-\frac{2}{3}} \left(\int_{\Omega} \det(|H(u)|)^{\frac{p}{2p+3}} \right)^{\frac{2p+3}{p}} \quad (19)$$

where here $H(u)$ is the true Hessian of u, $\Pi_h u$ the linear interpolate of u on H and C a constant that only depends on the quality (computed in M_{L^p}) of H. Note that Eq. (19) gives a practical way to control the level of error ε that is desired. Estimating the right-hand-side of Eq. (19) with $H_R(u_h)$ instead of $H(u)$ gives a first ε_0 error level so that to get an ε level of error, it is sufficient to scale (18):

$$M_{L^p}(u_h, \varepsilon) = \frac{\varepsilon_0}{\varepsilon} \det(|H_R(u_h)|)^{\frac{-1}{2p+3}} |H_R(u_h)| \quad (20)$$

In what follows, Feflo.a is used to adapt the mesh and compute the metric field from a user defined sensor. Pratical implementation and a detailed description can be found in Ref. [32].

IV. Numerical Simulation Setup

A. Aircraft configuration

The objective of the present work is to study the near-field of a jet/vortex interaction on a realistic aircraft configuration. However, such realistic aircraft geometries are ususally aircraft makers proprietary and, as such, difficult to use as a research platform as intended in this work. Therefore it was decided to use a well-known, well documented, open-source geometry: the Common Research Model designed by NASA and Boeing [30]. This configuration is representative of a Boeing 777. As depicted in Fig. 2, all elements of the CRM were included in the present work: wing, fuselage, nacelle, pylon, horizontal tail plane (HTP) and vertical tail plane (VTP). Note that the

VTP was designed by ONERA and shared with the community, see Ref. [31][32].The design of an internal engine geometry to simulate a dual stream jet and the trimming of the HTP were necessary to produce a representative aircraft configuration for the present study. Those preliminary operations were carried out using the CRM structured grids provided by the Drag Prediction Workshop, using the chimera approach and the elsA software [33].

Fig. 2 Original CRM/LRM configuration with Through Flow Nacelle

Indeed, the nacelle of the CRM is a trough flow nacelle, as commonly used for wind-tunnel tests when the influence of the powerplant integration needs to be simulated. For the purposes of the present work, a dedicated internal engine geometry was designed to allow the simulation of a dual-stream jet in the RANS computations, as illustrated in Fig. 3. Note that a similar approach was carried out in Ref. [34], unfortunately this previous work did not fit the purpose of our study and a new interior engine design was created.

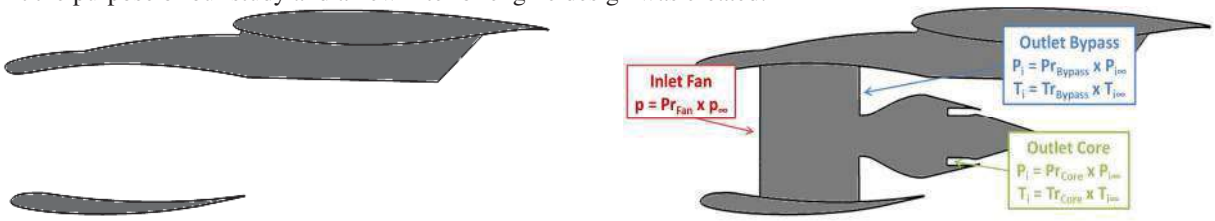

(a) Original Through Flow Nacelle of the CRM *(b) Internal engine designed*

Fig. 3 Modification of the CRM nacelle to simulate bypass and core jet flows

As shown in Fig. 3b, the engine inlet, secondary outlet and primary outlet are managed by boundary conditions based on pressure and temperature ratios which were set in order to balance the inlet and outlet mass flows, and most importantly to balance the drag and trust of the complete aircraft. The values of the boundary conditions are given in Table 2. The bypass ratio of the designed engine is of 12 which is representative of modern aircraft engines.

Tab 1 Engine parameters used

Pr_{Fan}	Pr_{Bypass}	Tr_{Bypass}	Pr_{Core}	Tr_{Core}
1.4	1.63	1.16	1.25	2.45

Eventually, the HTP was trimmed in order to ensure that the pitching moment of the aircraft is null, as one would expect from an aircraft in cruise conditions. The final geometry of the configuration studied in the following is illustrated in Fig. 4 and Fig. 5.

Fig. 4 CRM wing/body/engine geometry used in the simulations, highlighting engine primary core (red) and bypass flow (orange)

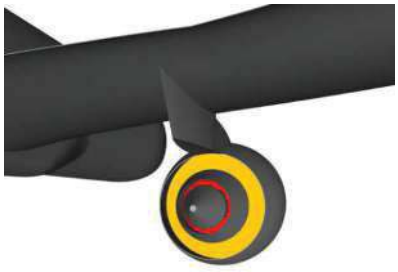

Fig. 5 Close-up of the engine primary core (red) and bypass flow (orange)

B. Computational domain, boundary and initial conditions

The aircraft is assumed to be operating under typical cruise conditions, either from an atmospheric point of view or from the engine emissions and exhaust-gas temperature. Tab. 2 presents the data used in the numerical simulations. The initial atmospheric conditions were chosen so that a contrail was expected to form in the plume. The ambient temperature was set at 223 K and pressure at 264 hPa to simulate cruise conditions at an altitude of about 34,000 ft. Relative humidity with respect to liquid water was set at 60 % (relative humidity with respect to ice corresponding to 100%) in order to fulfill the Schmidt–Appleman criterion at the selected ambient temperature [2]. Tab. 3 sums up the computational domaine. The span b in the CRM case is around 60 m long.

Tab. 2 Common atmospheric conditions and engine-exhaust characteristics

Flight Conditions				Engine Core Flow			Engine Bypass Flow		
Temperature (K)	Velocity (m/s)	Pressure (hPa)	Relative Humidity (%)	Total Temperature (K)	Total Pressure (Pa)	Soot ($/m^3$)	Total Temperature (K)	Total pressure (Pa)	Soot ($/cm^3$)
223.15	254.38	264.37	60	626.41	530.01	10^{12}	297.23	699.61	0

Tab. 3 computational domain

Domain Size	L_x	$[-10b; 20b]$
	L_y	$[0; 10b]$
	L_z	$[-10b; 10b]$
Boundary Conditions	*x=-10b*	Inlet
	x=20b	Outlet
	y=0	Symmetry
	y=10b	Outlet
	z=-10b	Slip (normal stress set to 0)
	z=10b	Slip (normal stress set to 0)

The engine-core-flow and bypass-flow properties were taken from Ref. [35] for the CFM56-3. Tab. 4 presents the initial condition used for the species mass-fractions according to Ref. [35] for core engine exhaust and Ref. [20] for the ambient air.

Tab. 4 Initial condition for the main species

Species		Mass Fraction	
k	**Molecular Name**	**Exhaust Core**	**Ambient Air**
1	*O*	0.00	0.00
2	O_2	$1.49\text{x}10^{-1}$	$2.32\text{x}10^{-1}$
3	O_3	0.00	$4.97\text{x}10^{-7}$
4	*H*	0.00	0.00
5	H_2	0.00	$6.26\text{x}10^{-8}$
6	*OH*	$5.93\text{x}10^{-6}$	0.00
7	HO_2	0.00	0.00
8	H_2O	$2.20\text{x}10^{-2}$	$6.08\text{x}10^{-5}$
9	H_2O_2	0.00	0.00
10	*NO*	$6.90\text{x}10^{-5}$	0.00
11	NO_2	$1.06\text{x}10^{-5}$	0.00
12	NO_3	0.00	0.00
13	N_2O_5	0.00	0.00
14	HNO_2	0.00	0.00
15	HNO_3	0.00	0.00
16	*CO*	$2.90\text{x}10^{-5}$	$3.87\text{x}10^{-8}$
17	CO_2	$4.82\text{x}10^{-2}$	$5.01\text{x}10^{-4}$
18	*SO*	0.00	0.00
19	SO_2	$1.15\text{x}10^{-5}$	0.00
20	SO_3	0.00	0.00
21	HSO_3	0.00	0.00
22	H_2SO_4	0.00	0.00

Species		Mass Fraction	
k	Molecular Name	Exhaust Core	Ambient Air
23	N_2	$1-\sum_{k=1}^{22} y_k$	$1-\sum_{k=1}^{22} y_k$

V. Results and discussion

A. Grid mesh adaptation

As said previously, a large range of space and time scales, from the engine exit to the atmospheric global scale is needed to deal with contrails formation. The main difficulty here, in this kind of simulation, is that you need to anticipate the zones in the computational domain where grid points are required.

According to the adaptative algorithm described in section III, several successive meshes have been generated. Tab. 5 presents an overview of the properties of the 5 meshes used. The number of prism and pyramid elements remains the same because the adaptive algorithm is only applied to tetrahedron elements. The mesh #1 corresponds to an initial mesh provided by the user without taking into account any specific refined zone in the volume, except the boundary layer zone refinement with prism elements. This is typically the kind of mesh that would be used to compute aircraft performances.

Tab. 5 Overview of the grid mesh properties

Element type	Mesh #1	Mesh #2	Mesh #3	Mesh #4	Mesh #5
Tetrahedron	6,701,472	4,140,630	4,514,154	5,380,312	7,219,502
Prism	13,143,807				
Pyramid	95,668				

Fig. 6 to Fig. 9 illustrate the first step of the mesh adaptation based on the cross flow velocity field $\sqrt{u_2^2+u_3^2}$. For the mesh adaptation mechanics, the L^2 norm of the cross velocities is used as sensor. The Hessian is recovered using an L^2 projection scheme. For the different sequences of meshes, an increased complexity N is prescribed. Two cut plane have been done to show the effect of the adaptative algorithm: a first one at 1 span downstream of the wingtip and a second one at about 19 span downstream (the exit of the computational domain). As expected and shown, the final mesh generated (mesh #5) is well refined in the wingtip vortex and vortex sheet downstream of the wing, which is of primary importance in order to accurately capture the wingtip vortex evolution and roll-up. The extension of the refinement seems to be well propagated in the whole computational domain.

An overview of results are given in Fig. 10 to Fig. 21. These figures present cut planes, at various distances downstream of the wingtip (1, 4, 8, 12, 16 and 19 span), for 5 meshes generated by the algorithm, based on the cross flow velocity field, and the temperature field associated. The first column corresponds to the mesh #1, the second column, to mesh #2 and so on.

At 1 span downstream of the wingtip, Fig. 10 illustrates the refinement of the mesh and the zone of interest detected while Fig. 11 shows the temperature field. Clearly, from the left to the right, the structure of temperature field is becoming less coarse and more detailed: almost nothing seen on the mesh #1 and nearly no evolution between mesh #4 and #5. The temperature field reveals a wingtip vortex created, a hot spot due to the exhaust jet and another vortex due to the HTP.

At 4 span downstream of the wingtip, Fig. 12 and Fig. 13 confirm this trend: the refinement of the mesh and the zone of interest detected is really well capted. Once again, from the left to the right, the structure of temperature field is becoming quite detailed: almost nothing seen on the mesh #1 and nearly no evolution between mesh #4 and #5. The temperature field still reveals a wingtip vortex created, a hot spot due to the exhaust jet and another vortex due to the HTP.

All these results show the efficiency and the relevance of the mesh refinement algorithm which allows to capture the salient features of the vortical flow in the wake of the aircraft, but also the jet stream and the interaction between the vortex and the jet.

This capability is really of great importance when you are studying contrail formation. Indeed, as already said before, contrail formation and its evolution are complex processes leading to a spatially inhomogeneous distribution of gaseous constituents and primary particles, whose evolution is lead by thermodynamic conditions and aircraft parameters.

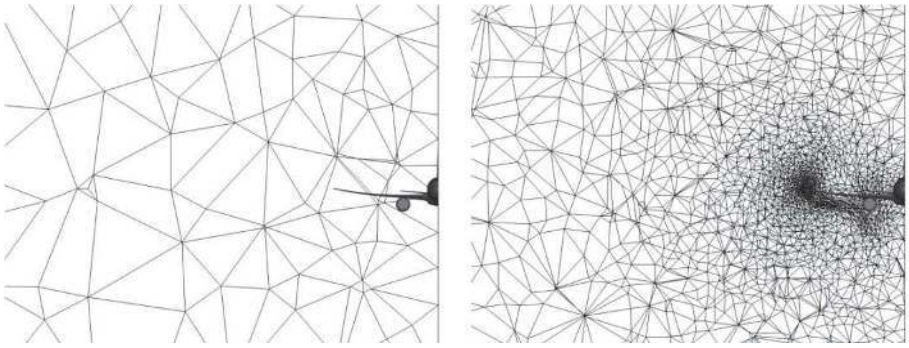

Fig. 6 First step mesh adaptation - cut plane at one span downstream of the wingtip : mesh #1 (left), mesh #2 (right)

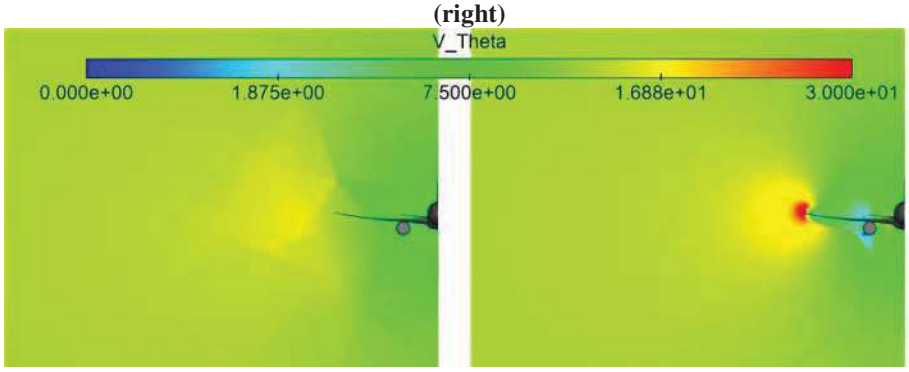

Fig. 7 Cross velocity field at one span downstream of the wingtip corresponding to mesh #1 (left) and mesh #2 (right

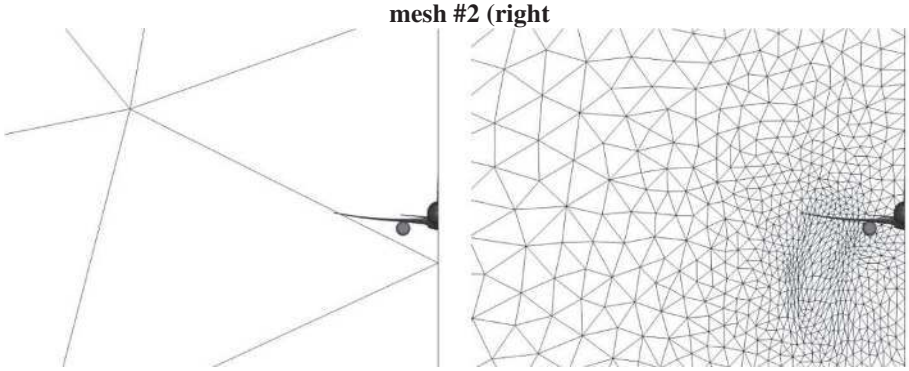

Fig. 8 First step mesh adaptation - cut plane at about 19 span downstream of the wingtip : mesh #1 (left), mesh #2 (right)

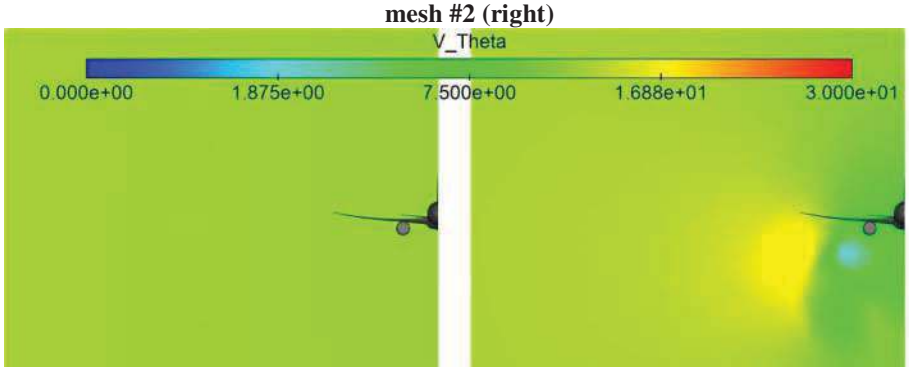

Fig. 9 Cross velocity field at about 19 span downstream of the wingtip corresponding to mesh #1 (left) and mesh #2 (right)

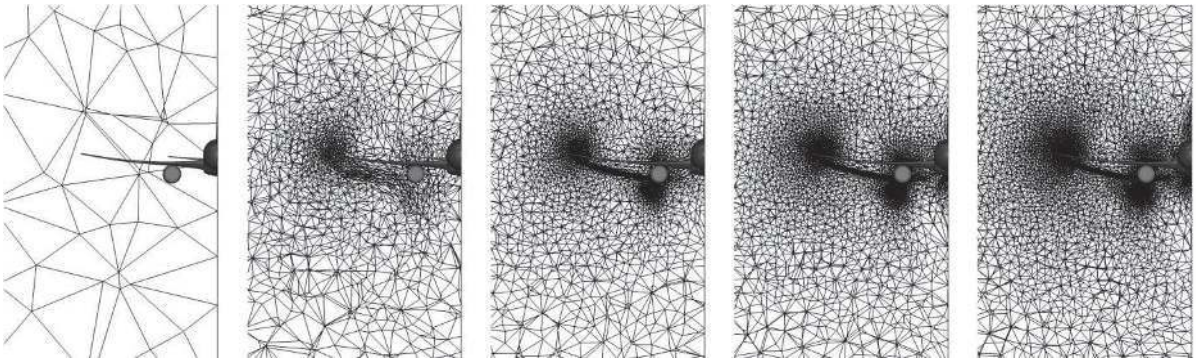

Fig. 10 Cut plane at 1 span downstream of the wingtip: mesh #1 to #5 from left to right side

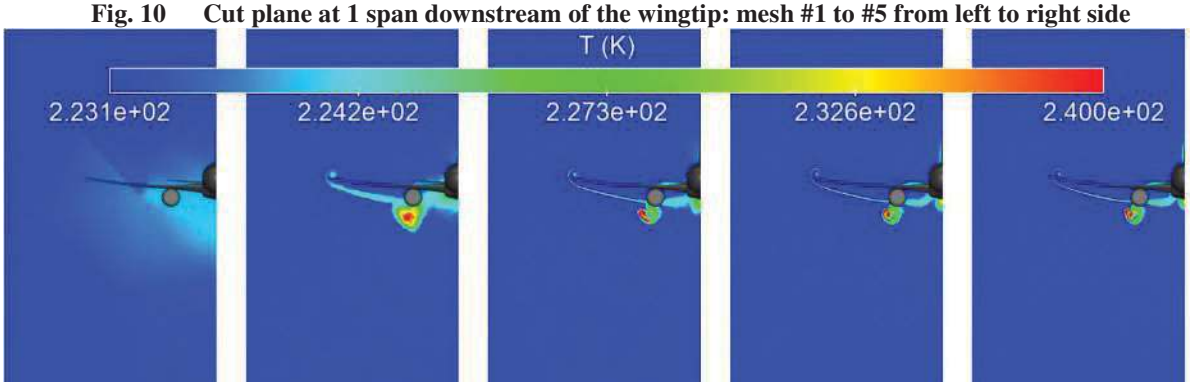

Fig. 11 Temperature field – Cut plane at 1 span downstream of the wingtip : mesh #1 to #5 from left to right side

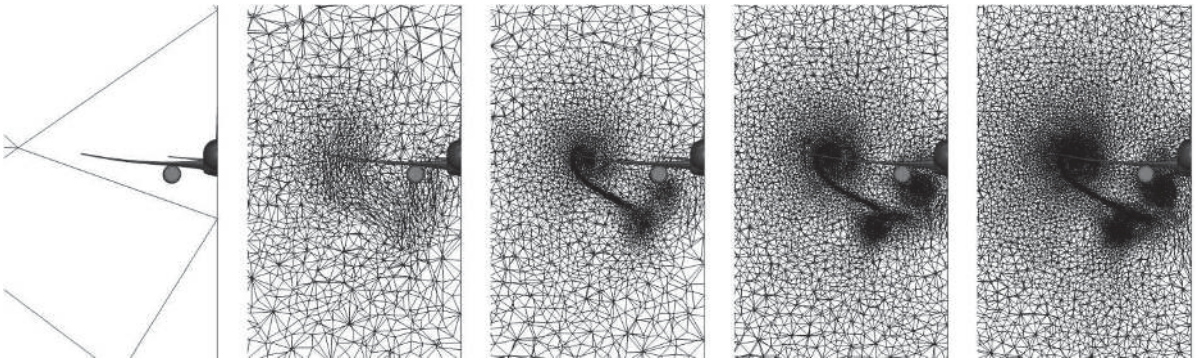

Fig. 12 Cut plane at 4 span downstream of the wingtip: mesh #1 to #5 from left to right side

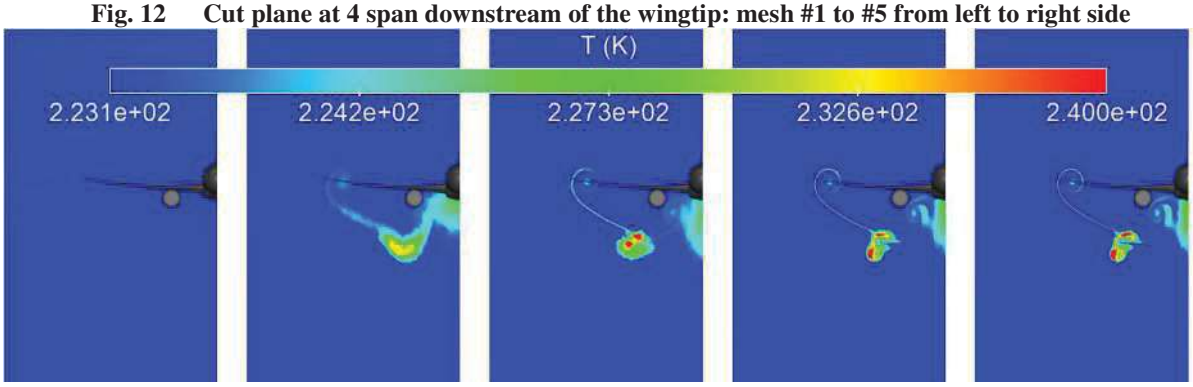

Fig. 13 Temperature field – Cut plane at 4 span downstream of the wingtip : mesh #1 to #5 from left to right side

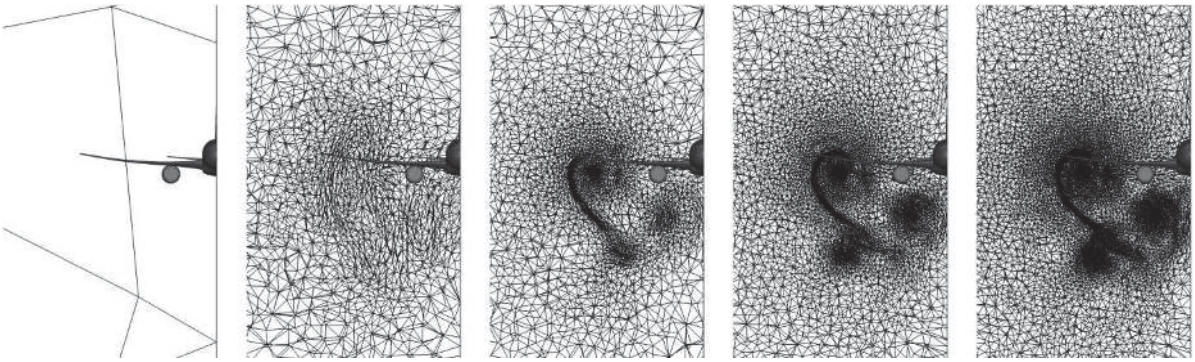

Fig. 14 Cut plane at 8 span downstream of the wingtip: mesh #1 to #5 from left to right side

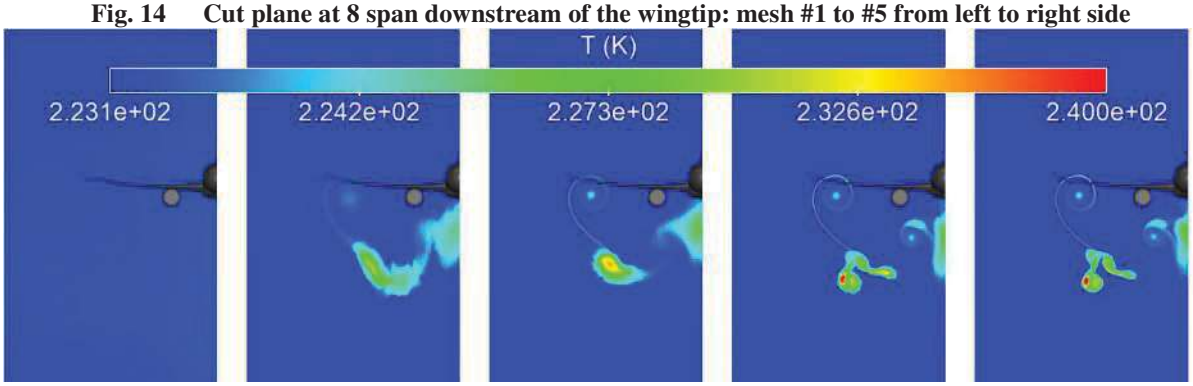

Fig. 15 Temperature field – Cut plane at 8 span behind the wingtip : mesh #1 to #5 from left to right side

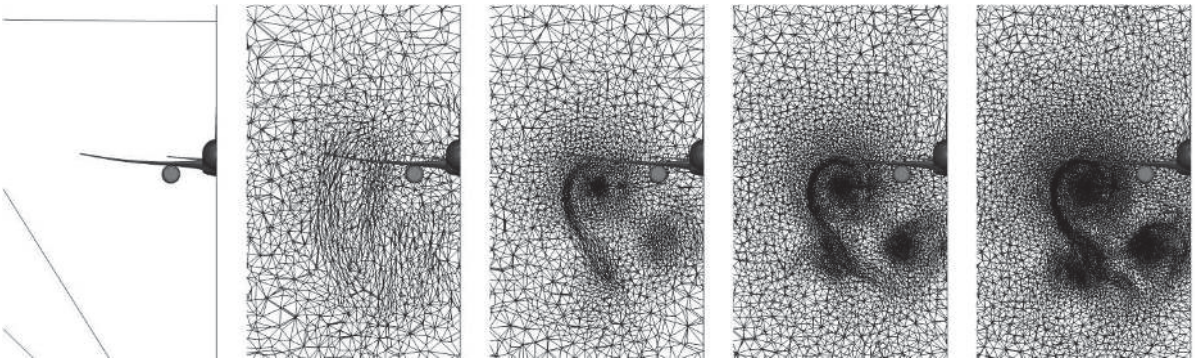

Fig. 16 Cut plane at 12 span behind the wingtip: mesh #1 to #5 from left to right side

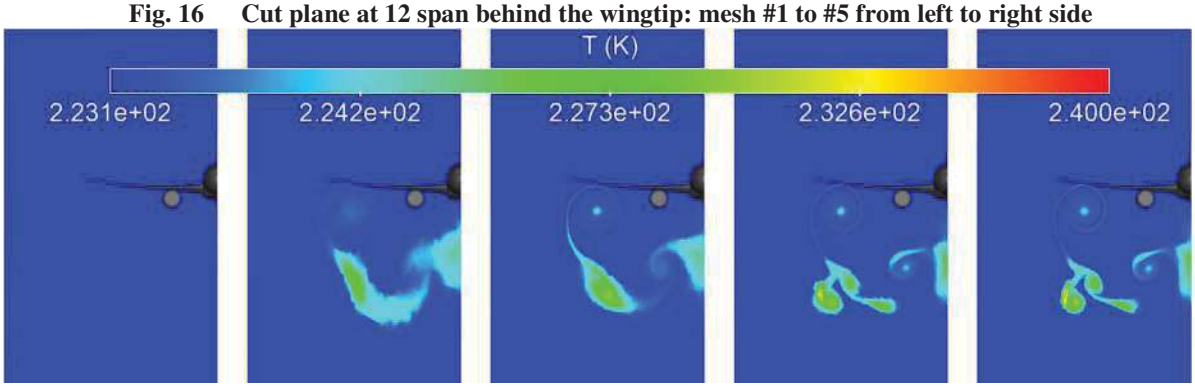

Fig. 17 Temperature field – Cut plane at 12 span behind the wingtip : mesh #1 to #5 from left to right side

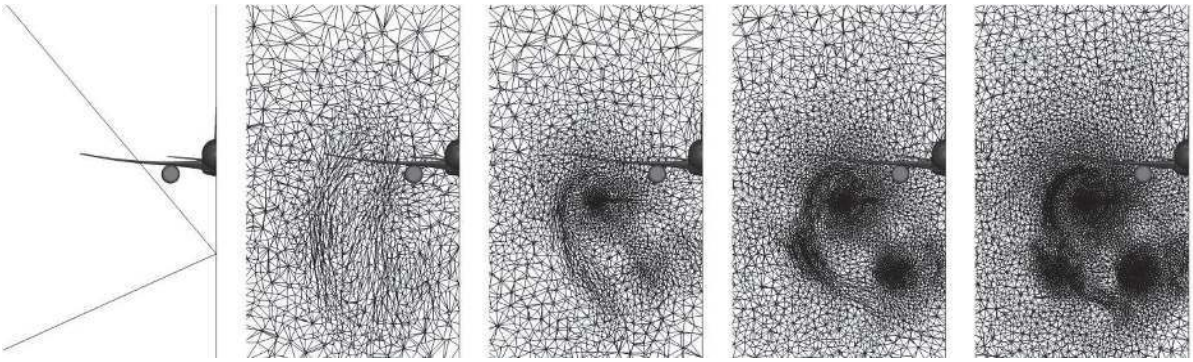

Fig. 18 Cut plane at 16 span downstream of the wingtip: mesh #1 to #5 from left to right side

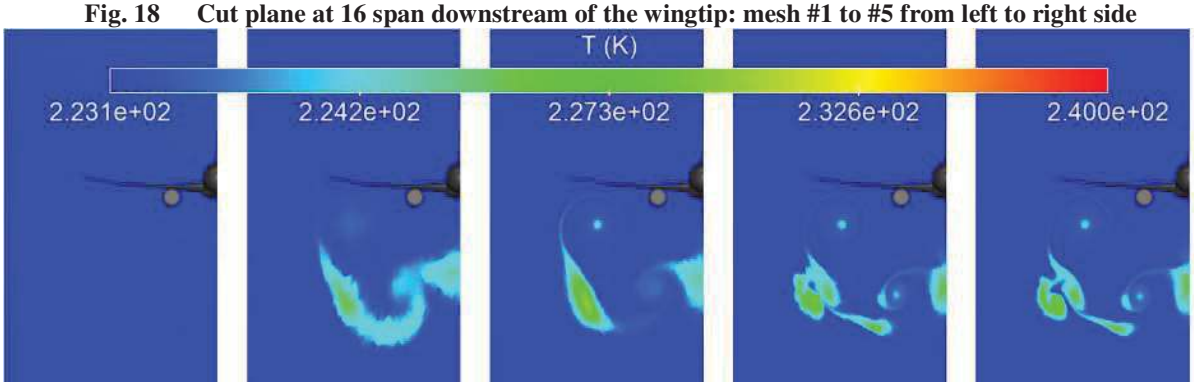

Fig. 19 Temperature field – Cut plane at 16 span downstream of the wingtip : mesh #1 to #5 from left to right side

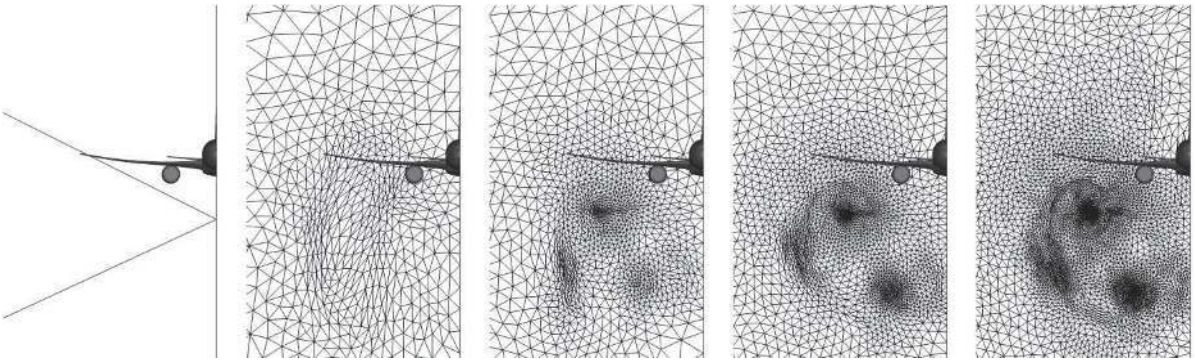

Fig. 20 Cut plane at about 19 span downstream of the wingtip: mesh #1 to #5 from left to right side

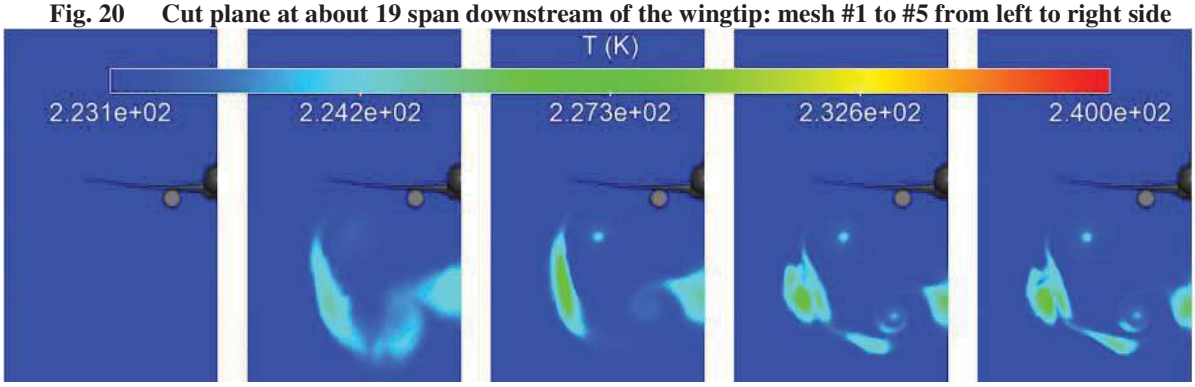

Fig. 21 Temperature field – Cut plane at about 19 span downstream of the wingtip : mesh #1 to #5 from left to right side

B. Jet/vortex dynamics

In Fig. 22, the streamlines point out the vortices and the jet development but also their interactions in the full computational domain (19b, i.e., nearly 1 km downstream the wingtip). It is also possible to identify the core and bypass streams interactions with the wing tip vortex. As expected, the vortices created by the wing tip and the HTP can be seen. The wingtip vortices (in blue) come closest and go down, which is an expected behavior. The hot jets also appears to be drained and cooled down by the wingtip vortices.

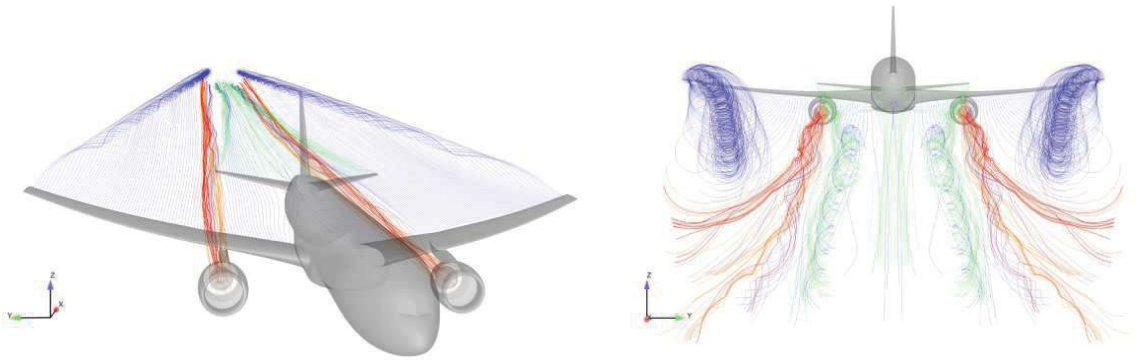

Fig. 22 Streamlines colored by element on aircraft: wing in blue, HTP in green, engine core flow in red and engine bypass in orange

According to Ref. [37][38], the distance between the two vortices should tend to the value $\frac{\pi}{4}b$ which corresponds to approximately 47.1 m. Tab. 6 presents the coordinates of the center of the wingtip vortex (x_c,y_c,z_c) for several distances behind the wingtip (1 to 17 span downstream of the wingtip). In this present case, this distance corresponds to $2y_c$, i.e. 45.4 m which is a good agreement with respect to the target distance.

Tab. 6 Coordinates of the center of the wingtip vortex

x_c	1.0b	2.0b	3.0b	4.0b	5.0b	6.0b	7.0b	8.0b	9.0b	10.0b	11.0b	12.0b	13.0b	14.0b	15.0b	16.0b	17.0b
y_c	27.3	26.3	25.5	24.9	24.5	24.2	23.9	23.6	23.5	23.3	23.2	23.1	23.0	23.0	22.9	22.8	22.7
z_c	5.9	5.9	5.6	5.3	4.8	4.3	3.7	3.1	2.6	2.1	1.6	1.1	0.6	0.1	-0.4	-1	-1.6

Due to the lack of experimental data for such complex case, a in-depth validation of the present simulation cannot be performed. However, the qualitative analysis performed above tends to show that the general behavior of the aircraft wake is correctly reproduced in the simulation.

C. Gas-phase chemistry and contrail formation

As already said, sulfur products are really important for contrail formation (aerosol precursors, activation of soot-particle, …). In the engine, sulfur is oxidized and forms sulfur dioxide (SO_2), which is further oxidized in the fresh plume to form SO_3 and H_2SO_4. The evolution of the sulfur products are given by the following reactions that are taking into account the present study:

$$SO_2 + OH \overset{M}{\rightleftharpoons} HSO_3 \quad (21)$$

$$HSO_3 + O_2 \rightleftharpoons SO_3 + HO_2 \quad (22)$$

$$SO_3 + H_2O \overset{M}{\rightleftharpoons} H_2SO_4 \quad (23)$$

Fig. 23, Fig. 24 and Fig. 25 present respectively, the mass fraction field of the sulfur products (SO_2, SO_3 and H_2SO_4), in a cut plane corresponding to the symmetry plan of the engine. According to Ref. [35] (see Tab. 4), initial conditions for the sulfur products have been choosen to be representative of a CFM56-3 engine. As expected, the maximum of SO_3 concentration is observed very close to the engine-core-flow exit. It is mainly due to the efficiency of the reaction Eq. (22) that converts HSO_3 into SO_3.

However, it is important to note that the plume is highly tri-dimensionnal. So, the fact that the concentration of the sulfur species tends to zero, is misleading: the cut plane after few meters does not intersect the zone that contains the sulfur species. Fig. 26 present the mass fraction field of SO_3 (from left engine) and H_2SO_4 (from right engine), at several local downstream of the wingtip (0.5b, 4b, 8b, 12b, 16b and 19b). Streamlines (purple line) coming from the

engine core flow, are also plotted in order to locate the mean position of the jet. This figure shows that SO_3 has fully disappeared 16 span downstream of the wingtip while H_2SO_4 is still drained by the wingtip vortices. As expected, the evolution of the sulfur species is mainly due to the entrainment of the ambient air and the dilution of the plume: initial sulfur species concentration was set to zero in the expanding plume. It is clear that both the wingtip of the wing and the HTP has a strong influence on the expansion of the plume.

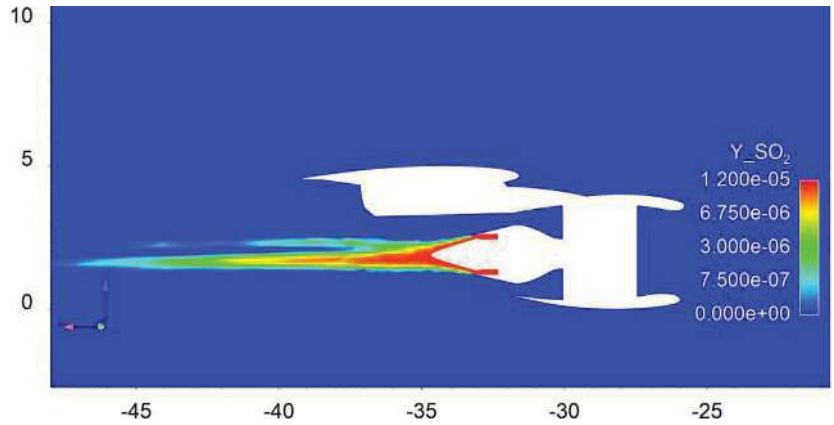

Fig. 23 Cut plane in the symmetry plan of the engine: mass fraction field of SO_2

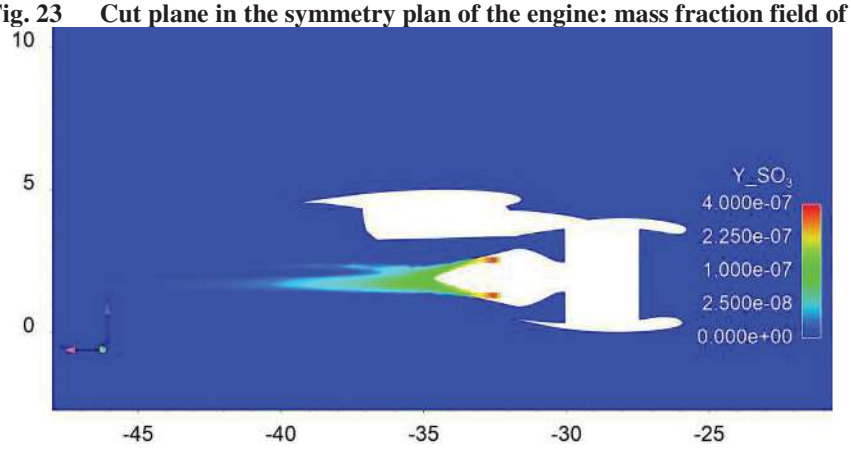

Fig. 24 Cut plane in the symmetry plan of the engine: mass fraction field of SO_3

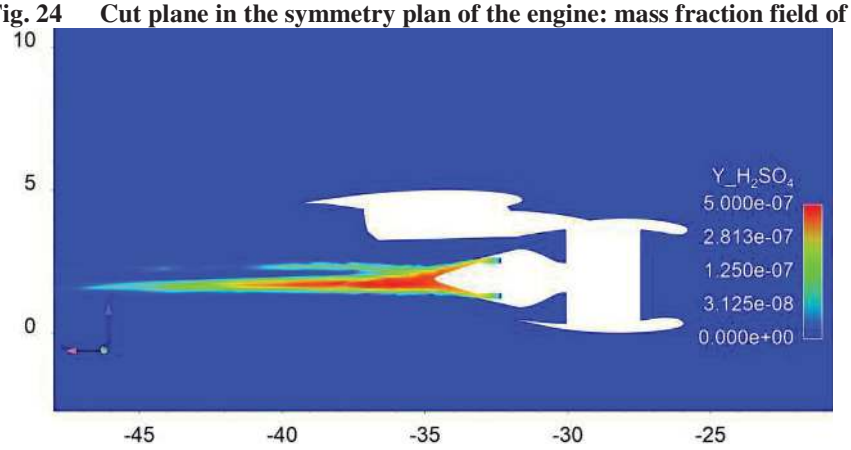

Fig. 25 Cut plane in the symmetry plan of the engine: mass fraction field of H_2SO_4

Fig. 27 presents the contrail highlighting based on the ice crystals particle radius above 100 nm. The extension of the contrail obtained thanks to the microphysical model, is reaching the end of the computational domain. In a first stage (first 10 span downstream of the wingtip), the contrail simulated is expanding within the plume and then, in a second stage, it remains stable and does not expand anymore. It is coherent with the observation.

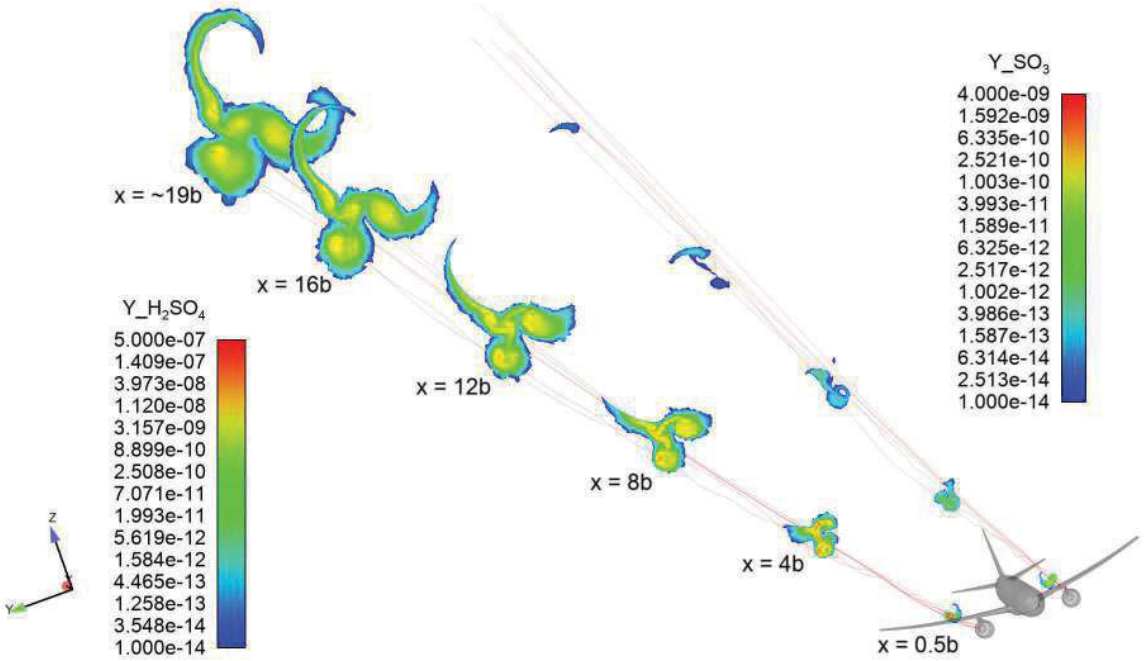

Fig. 26 Cut-plane at several distance behind the wingtip of mass fraction field for H_2SO_4 and SO_3.

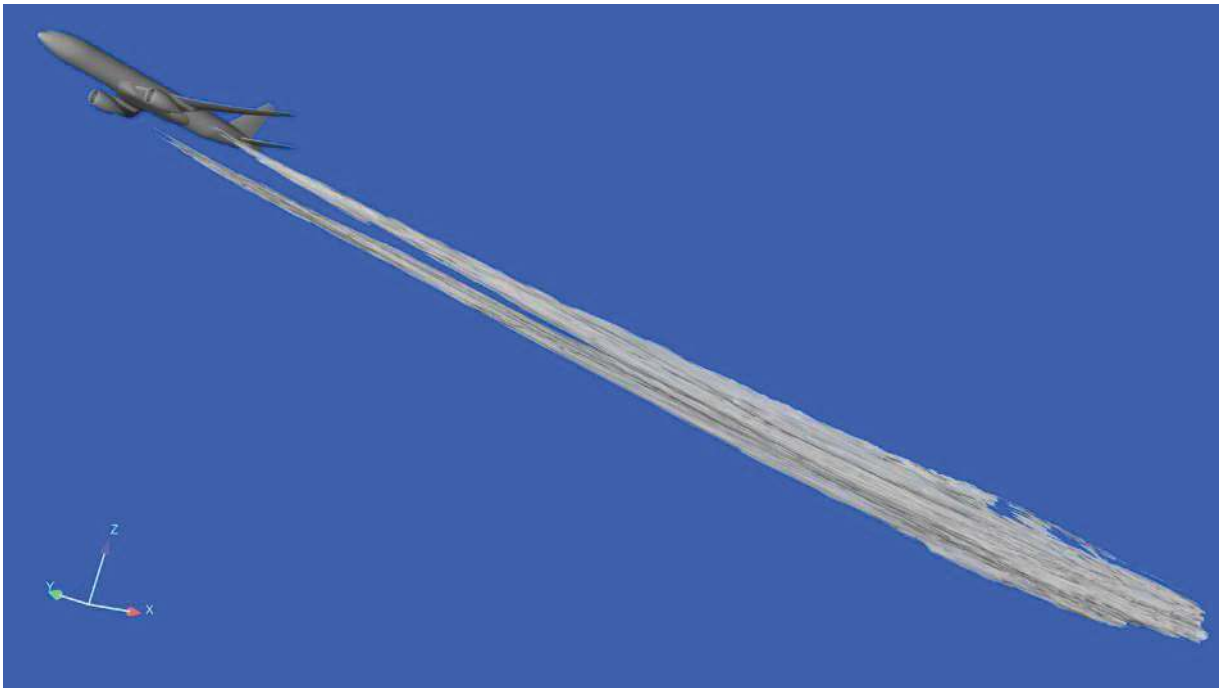

Fig. 27 Contrail highlighting based on ice crystals particle radius above 100 nm

VI. Conclusion

In this work, a 3-D RANS CFD approach with gas-phase chemistry, microphysical model and a mesh adaptation procedure have been used with success in order to simulate the formation and the evolution of contrails for typical cruise conditions, up to nearly 19 span (i.e. 1 km) downstream of the wingtip. Numerical simulations using a realistic aircraft configuration, based on the Common Research Model with wing, fuselage, nacelle, pylon,

horizontal tail plane (HTP) and vertical tail plane (VTP) have been carried out. A dedicated internal engine geometry has been designed to allow the simulation of dual-stream jet in the RANS computations. In addition, a gas-phase chemistry reaction scheme of 23 species and 60 reaction has been included and coupled with a microphysical model in order to account for soot and sulfur species interactions, but also for ice-crystal formation and growth. The mesh refinement procedure allows to recover the main feature of the vortex system downstream of the wake and the hot jet. Thanks to this procedure, it is then possible to track the plume evolution strongly linked to the wake and the hot jet evolution.

Since no experimental nor in-flight measurement are available to validate the numerical results for such complex case, a qualitative aerodynamic and gas-phase chemistry analysis has been performed to ensure the representativity of the evolution of the aircraft wake.

The main perspectives to be explored in the future are the inclusion of volatile-particle microphysics, but also the influence of the aircraft installation issues such as the pylon, the HTP and the engine position. Indeed, the results shows some effects in the jet/vortex dynamics but it is not clear to quantify how it affects the contrail formation, for example, and how it is important or not to take it into account. Other activation pathways through soot-vapor interactions could also be including the effect of organic compounds and the oxidation of soot-surface functional chemical groups, but these need further research before implementation. Another perspective is to explore LES or ZDES numerical approaches in order to catch instabilities such as Crow or Widnall instabilities.

Acknowledgments

The authors would like to acknowledge the French Civil Aviation (DGAC) for their funding in the frame of the PHYWAKE program.

References

[1] Lee, D. S., Pitari, G., Grewe, V., Gierens, K., Penner, J. E., Petzold, A., Prather, M. J., Schumann, U., Bais, A., Berntsen, T., Iachetti, D., Lim, L. L., and Sausen, R., "Transport impacts on atmosphere and climate: Aviation", *Atmos. Environ*., Vol. 44, 2010, pp. 4678–4734. doi: 10.1016/j.atmosenv.2009.06.00.

[2] Karcher, B, "Formation and radiative forcing of contrail cirrus", *Nature Communications*, 2018, Vol. 9, No 1824, doi:10.1038/s41467-018-04068-0.

[3] Schumann, U., "On conditions for contrail formation from aircraft exhausts", *Meteorol. Z*., Vol. 5, 1996, pp. 4–23.

[4] Schumann, U., Arnold, F., Busen, R., Curtius, J., Kärcher, B., Kiendler, A., Petzold, A., Schlager, H., Schröder, F., and Wohlfrom, K.-H., "Influence of fuel sulfur on the composition of aircraft exhaust plumes: the experiments SULFUR 1–7", J. *Geophys. Res*., 2002, Vol. 107, pp. 1719. doi: 10.1029/2001JD000813.

[5] Voigt, C., Schumann, U., Jurkat, T., Schauble, D., Schlager, H., Petzold, A., Gayet, J-F, Kramer, M., Schneider, J., Borrmann, S., Schmale, J., Jessberger, P., Hamburger, T., Lichtenstern, M., Scheibe, M., Gourbeyre, C., Meyer, J., Kubbeler, M., Frey, W., Kalesse, H., Butler, T., Lawrence, M.G., Holzäpfel, F., Arnold, F., Wendisch, M., Dopelheuer, A., Gottschaldt, K., Baumann, R., Zoger, M., Solch, I., Rautenhaus, M., and Dornbrack, A., "In-situ observations of young contrails - overview and selected results from the CONCERT campaign.", *Atmos. Chem. Phys*., 2010, Vol. 10, pp. 9039–9056, doi: 10.5194/acp-10-9039-2010.

[6] Paoli, R., Nybelen, L., Picot, J., and Cariolle, D., "Effects of jet/vortex interaction on contrail formation in supersaturated conditions." , *Phys. Fluids*, 2013, Vol 25, 053305, doi: 10.1063/1.4807063.

[7] Garnier, F., Maglaras, E., Morency, F., and Vancassel, X., "Effect of Compressibility on Contrail Ice Particle Growth in an Engine Jet.", *Int. J. Turbo Jet-Engines*, 2014, Vol. 31, pp. 131–140, doi:10.1515/tjj-2013-0039.

[8] llen, D.C., Meza, O., and Huebsch, W.W., "Persistent contrails and contrail cirrus. Part I: Large-Eddy Simulation from Inception to Demise.", *J. Atmos. Sci*., 2014, Vol. 71, pp. 4399–4419, doi:10.1175/JAS-D-13-0316.1.

[9] Lewellen, D.C., "Persistent contrails and contrail cirrus. Part II: Full lifetime Behavior", *J. Atmos. Sci*., 2014, Vol 71, pp. 4420–4438, doi:10.1175/JAS-D-13-0317.1.

[10] Unterstrasser, S., "Large-eddy simulation study of contrail microphysics and geometry during the vortex phases and consequences on contrail-to-cirrus transition.", *J. Geophys. Res*., 2014, Vol. 119, pp. 7537–7555, doi:10.1002/2013JD021418.

[11] Picot, J., Paoli, R., Thouron, O., and Cariolle, D., "Large eddy simulation of contrail evolution in the vortex phase and its interaction with atmospheric turbulence.", *Atmos. Chem. Phys*., 2015, Vol. 15, pp. 7369–7389. doi:10.5194/acp-15-7369-2015.

[12] Unterstrasser, S., and Görsch, N., "Aircraft-type dependency of contrail evolution.", *J. Geophys. Res*., 2014, Vol. 119, pp. 14015–14027, doi:10.1002/2014JD022642.

[13] Guignery, F. , Montreuil, E., Thual, O., and Vancassel, X., "Contrail microphysics in the near wake of a realistic wing through RANS", *Aerospace Science and Technology*, 2012, Vol. 23, No 1, pp 399–408, doi:10.1016/j.ast.2011.09.011.

[14] Khou, J.C., Ghedhaïfi, W., Vancassel, X., and Garnier, F., "Spatial Simulation of Contrail Formation in Near-Field of Commercial Aircraft.", *J. Aircraft*, 2015, Vol. 52, pp. 1927–1938.

[15] Wong, H., Yelvington, P.E., Timko, M.T., Onasch, T.B., Miake-Lye, R.C., Zhang, J., and Waitz, I.A., 2008: "Microphysical Modeling of Ground-Level Aircraft-Emitted Aerosol Formation: Roles of Sulfur-Containing Species.", *J. Prop. Power*, Vol. 24, pp. 590–602. doi:10.2514/1.32293.

[16] Jensen, E.J., Toon, O.B., Kinne, S., Sachse, G.W., Anderson, B.E., Roland Chan, K., Twohy, C.H., Gandrud, B., Heymsfield, A., and Miake-Lye, R.C., "Environmental conditions required for contrail formation and persistence.", *J. Geophys. Res.*, 1998, Vol. 103, pp. 3929–3936
[17] Refloch, A., Courbet, B., Murrone, A., Villedieu, P., Laurent, C., Gilbank, P., Troyes J., Tessé, L., Chaineray, G., Dargaud, J.B., Quémerais, E., and Vuillot, F., "Cedre Software.", *Aerosp. Lab J.*, 2011, pp. 1–10**.**
[18] Menter, F., "Two-equation eddy-viscosity turbulence models for engineering applications", *AIAA Journal*, 1994, Vol. 32, No 8, pp. 1598-1605, doi:10.2514/3.12149.
[19] Kärcher, B., "Physicochemistry of aircraft-generated liquid aerosols, soot, and ice particles: 1. Model description.", *J. Geophys. Res*., 1998, Vol. 103, pp. 17111–17128, doi: 10.1029/98JD01044.
[20] Kärcher, B., Hirschberg, M.M., and Fabian, P., "Smallscale chemical evolution of aircraft exhaust species at cruising altitudes.", *J. Geophys. Res*., 1996a, Vol. 101, doi:10.1029/96JD01059.
[21] Kärcher, B., Peter, T., Biermann, U.M., and Schumann, U., 1996b: "The Initial Composition of Jet Condensation Trails", *J. Atmospheric Sci*., 1996b, Vol. 53, pp. 3066–3083, doi: 10.1175/1520-0469(1996)053<3066:TICOJC>2.0.CO;2
[22] Bottasso, C. L., "Anisotropic mesh adaption by metric-driven optimization.", *Int. J. Numer. Meth. Engng*, 2004, Vol. 60, pp. 597–639.
[23] Castro-Dıaz, M. J., Hecht, F., Mohammadi, B., and Pironneau, O., "Anisotropic unstructured mesh adaptation for flow simulations.", *Int. J. Numer. Meth. Fluids*, 1997, Vol. 25, pp 475–491.
[24] Loseille, A., Alauzet, F., Dervieux, A., and Frey, P. J., "Achievement of second order mesh convergence for discontinuous flows with adapted unstructured mesh adaptation.", AIAA Paper 07-4186, 2007.
[25] Peraire, J., Vahdati, M., Morgan, K., and Zienkiewicz, O.C., "Adaptive remeshing for compressible flow computations.", *J. Comp. Phys*., 1987, Vol. 72, pp. 449–466.
[26] Schall, E., Leservoisier, D., Dervieux, A., and Koobus, B., "Mesh adaptation as a tool for certified computational aerodynamics.", *Int. J. Numer. Meth. Fluids*, 2004, Vol. 45, 179–196.
[27] Tam, A., Ait-Ali-Yahia, D., Robichaud, M. P., Moore, M., Kozel, V., and Habashi, W. G., "Anisotropic mesh adaptation for 3D flows on structured and unstructured grids.", *Comput. Meth. Appl. Mech. Engrg*., 2000, Vol. 189, pp. 1205–1230.
[28] Vallet, M.-G., Manole, C.-M., Dompierre, J., Dufour, S., and Guibault, F., "Numerical comparison of some hessian recovery techniques.", *Int. J. Numer. Meth. Engrg*., 2007, Vol. 72, pp. 987–1007.
[29] Loseille, A., Chapter 10 - *Unstructured Mesh Generation and Adaptation*, Editor(s): Rémi Abgrall, Chi-Wang Shu, In Handbook of Numerical Analysis, Elsevier, Vol. 18, pp. 263-302, 2017.
[30] Vassberg, J., DeHaan, M., Rivers, M., and Wahls, R., "Development of a Common Research Model for Applied CFD Validation Studies", AIAA Paper 2008-6919, 2008.
[31] Hue, D., Péron, S., Wiart, L., Atinault, O., Gournay, E., Raud, P., Benoit, C., and Mayeur, J., " Validation of a near-body and off-body grid partitioning methodology for aircraft aerodynamic performance prediction", *Computers and Fluids*, 2015, Vol. 117, pp. 196-211, doi:10.1016/j.compfluid.2015.05.021.
[32] Cartieri, A., Hue, D., Chanzy, Q., and Atinault, O., "Experimental Investigations on Common Research Model at ONERA-S1MA–Drag Prediction Workshop Numerical Results", Journal of Aircraft [online database], https://doi.org/10.2514/1.C034414 [retrieved 5 July 2017].
[33] Cambier, L.; Heib, S., and Plot, S. "The Onera elsA CFD software: input from research and feedback from industry", *Mechanics and Industry*, 2013, Vol. 14, pp. 159-174, doi:10.1051/meca/2013056.
[34] Blumenthal, B., Elmiligui, A., Geiselhart, K. and Campbell, R., "Computational Investigation of a Boundary-Layer Ingesting Propulsion System for the Common Research Model", AIAA Paper 2016-3812, 2016, doi: 10.2514/6.2016-3812.
[35] Garnier, F., Baudoin, C., Woods, P., and Louisnard, N., "Engine emission alteration in the near field of an aircraft.", *Atmos. Env. Geophys. Res. Lett*., 1997, Vol. 31, No 12, pp. 1767-1781, doi:10.1016/S1352-2310(96)00329-9.
[36] Khou, J.C., Ghedhaïfi, W., Vancassel, X., Montreuil, E., and Garnier, F., "CFD simulation of contrail formation in the near field of a commercial aircraft: Effect of fuel sulfur content", *Meteorologische Zeitschrift*, 2017, doi:10.1127/metz/2016/0761.
[37] Betz, A., "Behavior of vortex systems.", NACA TM-713, 1933.
[38] Morfey, C.L., "A review of aircraft vortex wakes and their interaction with following aircraft", Institute of Sound and Vibration, Research Report, University of Southampton, Southampton, U.K, 1986.